Modulating Electric Field Distribution by Alkali Cations for CO_2 Electroreduction in Strongly Acidic Medium

Authors: Jun Gu [1,2], Shuo Liu [3], Weiyan Ni [1], Wenhao Ren [1], Sophia Haussener [3] and Xile Hu [1]*

Affiliation:

1. Laboratory of Inorganic Synthesis and Catalysis, Institute of Chemical Sciences and Engineering, Ecole Polytechnique Fédérale de Lausanne (EPFL), EPFL-ISIC-LSCI, BCH 3305, Lausanne, CH 1015 Switzerland.
2. Department of Chemistry, Southern University of Science and Technology, Shenzhen, Guangdong, 518055, China.
3. Laboratory of Renewable Energy Science and Engineering, Institute of Mechanical Engineering, École Polytechnique Fédérale de Lausanne, 1015 Lausanne, Switzerland.

* Corresponding author. E-mail: xile.hu@epfl.ch

Abstract: The reaction of carbon dioxide with hydroxide to form carbonate in near neutral or alkaline medium severely limits the energy and carbon efficiency of CO_2 electroreduction. Here we show that by suppressing the otherwise predominant hydrogen evolution using alkali cations, efficient CO_2 electroreduction can be conducted in acidic medium, overcoming the carbonate problem. The cation effects are general for three typical catalysts including carbon supported tin oxide, gold, and copper, leading to Faradaic efficiency of as high as 90% for formic acid and CO formation. Our analysis suggests hydrated alkali cations physisorbed on the cathode modify the distribution of electric field in the double layer, which impedes hydrogen evolution by suppressing the migration of hydronium ions while at the same time promotes CO_2 reduction by stabilizing key intermediates.

Introduction

Electrochemical reduction of CO_2 to produce chemicals and fuels is widely studied as a potential solution for renewable energy storage and CO_2 recycling.[1] Because the hydrogen evolution reaction (HER) dominates in acidic aqueous solutions, CO_2 electroreduction is conducted in an alkaline or near neutral medium.[2,3] These reaction media, however, create one of the most important obstacles for high-efficient steady-state CO_2 electrolysis: the facile reaction of CO_2 with hydroxide (OH^-) to form carbonate (CO_3^{2-})[4,5]. In alkaline medium, although the overpotentials of many catalysts are minimized[6,7], the carbonate problem obliges continuous refreshing of the OH^- electrolytes in a flow-cell configuration in order to obtain a stable performance.[2,3] The regeneration of CO_2 and 2 OH^- from aqueous carbonate is energy demanding and leads to a low or even negative energy efficiency for CO_2 electroreduction.[5,8] In near neutral media such as bicarbonate solutions, steady-state CO_2 electrolysis is possible.[9,10] However, CO_2 is still consumed by OH^- anions electrochemically generated in CO_2 electroreduction. The (bi)carbonate is protonated near the anode to regenerate CO_2, which leads to a low carbon efficiency.[11] In addition, in near neutral media the high resistance of the solution[12] as well as higher overpotential for oxygen evolution reaction (OER)[13] lead to a high cell voltage and low energy efficiency. In strongly acidic media the resistance and overpotential for OER are lower, and the carbonate problem can be solved since carbonate will not cross the medium to the anode. An acidic medium is also essential to obtain formic acid from CO_2 reduction. In near neutral and alkaline media, the same reduction leads to formate, which requires energy-intensive downstream processes for separation and conversion.

Efficient CO_2 electroreduction in an acidic medium is challenging because the HER is normally more facile than CO_2 reduction. It was reported that in CO_2-saturated 0.1 M $HClO_4$ solutions (pH =1), the Faradaic efficiency of HER was nearly 100% on Fe-N-C[7] and Au[14] catalysts, both of which are efficient CO_2 reduction catalysts in near neutral and alkaline media. CO_2 reduction to CO was feasible in mildly acidic media (pH $\geq$ 3) such as a mixed $HClO_4$-$NaClO_4$ solution[15] and a K_2HPO_4 solution.[14] Bondue *et al.* proposed that the HER was suppressed by OH^- anions generated from CO_2 reduction.[15] During the preparation of our publication, Huang et al. reported efficient CO_2 electroreduction on Cu catalysts in strongly acidic solutions (pH = 0.67) with H_3PO_4-KCl mixed electrolytes.[16] In both studies, alkali cations are essential for CO_2 reduction, but the mechanism of cation-promotion remains unclear. The very recent work of Monteiro *et al.* demonstrated alkali cations are indispensable for the stabilization of CO_2^- species, a key intermediate for CO_2 reduction.[17] However, how alkali

cations suppress the predominant HER in acidic media is unclear.

Here we demonstrate efficient CO_2 electroreduction with Faradaic efficiency as high as 90% in strongly acidic media (pH =1) by suppressing HER with alkali cations. This approach can be applied for three representative classes of catalysts, namely carbon supported SnO_2, Au, and Cu nanoparticles (SnO_2/C, Au/C and Cu/C, Supplementary Fig. 1), which give formic acid, CO, and hydrocarbons as main CO_2 reduction products, respectively. Our simulation and analysis indicate that the alkali cations in the double layer of the cathode effectively shield the electric field in the diffusion layer and suppress the migration of hydronium ions towards the cathode, which lowers the concentration of hydronium ions in the outer Helmholtz plane (OHP) and thus suppresses HER. Meanwhile the cations strengthen the field in the Stern layer and stabilize key intermediates in CO_2 reduction.

Results

CO_2 electroreduciton in acidic medium

The activity and selectivity of the CO_2 reduction reaction are sensitive to alkali metal cations in near neutral bicarbonate solutions.[14,18-20] Several hypotheses such as local pH effect[19] and electrostatic interaction[18,20] have been made to explain these cation effects. Inspired by these studies, we decided to explore a possible influence of alkali cations for CO_2 reduction vis-à-vis the HER in strongly acidic medium. We first probed the effect of K^+ for CO_2 reduction on SnO_2/C at pH = 1. We used a three-electrode flow cell with a gas diffusion electrode (GDE) as working electrode (Supplementary Fig. 2) for electrocatalytic tests. Fig. 1a shows the cyclic voltammetry (CV) curves of SnO_2/C in two different electrolyte solutions: an aqueous solution of 0.1 M trifluoromethanesulfonic acid (HOTf) and a solution containing 0.1 M HOTf + 0.4 M potassium trifluoromethanesulfonate (KOTf). HOTf is a strong acid and the addition of K^+ ions did not change the pH of the solution. The pH of both solutions was 1. HER was the only reaction under a N_2 atmosphere. The addition of K^+ greatly suppressed the HER as the potential was more negative than -0.8 V vs reversible hydrogen electrode (RHE) (blue and orange curves in Fig. 1a). In 0.1 M HOTf, the CV curves collected under N_2 and CO_2 were nearly identical, indicating the dominance of HER and the lack of CO_2 reduction in the presence of CO_2. Indeed, H_2 was the only reduction product when CO_2 was present (Supplementary Fig. 3). In the solution containing 0.1 M HOTf plus 0.4 M KOTf, a higher current density was observed in the CV curve with CO_2 at potentials more negative of -1.0 V vs RHE (green curve in Fig. 1a). Formic acid and CO were detected as products in this potential range (Supplementary Fig. 3).

Fig. 1b-g shows the performance of SnO_2/C, Au/C and Cu/C in electrolyte solutions containing 0.1 M H_2SO_4 + 0.4 M K_2SO_4 (pH = 1.5). This combination of electrolytes is more practical than the combination of HOTf + KOTf, even though addition of K^+ ions slightly changed the pH of H_2SO_4 solutions. For SnO_2/C, formic acid was the major product of CO_2 reduction. The maximum Faradaic efficiency and partial current density were 88% and 314 $mA \cdot cm^{-2}$, respectively (Fig. 1b, c). These performance metrics are comparable to state-of-the-art results of formic acid production from a solid-state electrolyzer[21] and formate formation in near neutral solutions[22]. Aqueous solution of formic acid could be separated from the electrolyte solution by distillation (Supplementary Fig. 4). This result demonstrated the advantage of an acidic reaction medium for formic acid generation compared to a near neutral or alkaline medium where only formate would be generated. For Au/C, CO was the major product with the maximum Faradaic efficiency and partial current density as 91% and 227 $mA \cdot cm^{-2}$, respectively (Fig. 1d, e). For Cu/C, formic acid, CO, methane, ethylene, propene, acetic acid, ethanol and 1-propanol were detected as the products of CO_2 reduction (Supplementary Fig. 5). The minimum Faradaic efficiency of HER was 16%, lower than that of Cu/PFSA catalyst (PFSA = perfluorosulfonic acid) in H_3PO_4-KCl medium (Faradaic efficiency of HER = 36%) reported by Huang et al.[16] Among the products of > 2e reduction, ethylene was the major product with the partial current density of 136 $mA \cdot cm^{-2}$ (Fig. 1g). Its Faradaic efficiency was 25% (Fig. 1f), similar to the highest Faradaic efficiency for ethylene production on Cu/PFSA in H_3PO_4-KCl medium by Huang et al.[16] The maximum partial current densities of CO formation on Au/C and ethylene formation on Cu/C in acidic media were comparable to those on state-of-the-art catalysts in near neutral and alkaline media.[2,3,23,24]

We also compared the performances of Au/C in CO_2 electroreduction in acidic (0.1 M H_2SO_4 + 0.4 M K_2SO_4), near neutral (0.8 M $KHCO_3$) and alkaline (0.8 M KOH) media in a two-electrode cell (Supplementary Fig. 6). As expected, the carbonate problem was severe in an alkaline medium: While the initial cell voltage was low, it increased substantially (by 34%) in 2.5 h (Fig. 2a). Meanwhile, the pH of the solution decreased from 13.5 to 8.1 due to the reaction of OH^- with CO_2 (Fig. 2b). In near neutral and acidic media, the cell voltages were largely stable (Fig. 2a), as no net reaction between electrolyte and CO_2 occurred in these media. The pH of the solutions remained stable after 4 h of electrolysis (Fig. 2b). The overall cell voltage with the acidic medium was about 0.3 V lower than that with the near neutral medium for 200 $mA \cdot cm^{-2}$ at 4 h. For SnO_2/C and Cu/C catalysts, inductively coupled plasma-mass spectrum (ICP-MS) was used to measure the dissolution of metal into the electrolyte solution

during electrolysis (Supplementary Table 1). 1.70% of Sn and 0.27% of Cu were dissolved in acidic medium after 4 h of electrolysis at 200 $mA \cdot cm^{-2}$. The dissolution ratios were lower in near neutral and alkaline media (Supplementary Table 1). Nevertheless, the majority of SnO_2/C and Cu/C catalysts remained stable. The size distributions of Sn and Cu nanoparticles after electrolysis were similar to those of the as-prepared catalysts (Supplementary Fig. 7).

Carbon and energy efficiency

Table 1 summarizes the theoretical carbon efficiency of CO_2 electroreduction to generate different products in a flow cell in acidic, near neutral, or alkaline medium, and a membrane-electrode-assembly (MEA) setup with an anion exchange membrane. In alkaline medium, the constant reaction of CO_2 with OH^- leads to a carbon efficiency of around 10% or lower.[2,25,26] In near neutral medium and in an MEA setup, CO_2 reacts with OH^- generated at the cathode (CO_2 reduction), forming carbonate ions. The latter cross the electrolyte solution or the membrane to the anode where they react with H^+ generated by OER (Supplementary Fig. 8b). In 2e-reduction to form CO or formate, 50% of CO_2 is consumed to form carbonate; in the case of ethylene production, 75% of CO_2 is consumed to form carbonate.[5,11] Indeed, in the reduction of CO_2 to CO on Au in near neutral medium, a large amount of CO_2 was detected in the gas generated at the anode (Supplementary Fig. 9), in agreement with the above analysis. In contrast, the theoretical carbon efficiency in acidic medium is up to 100%, which is supported by the fact that CO_2 was not detected in the gas product at the anode in CO_2 electroreduction on Au in acidic medium (Supplementary Fig. 9). Note that a crossover of formate through an anion exchange membrane in a flow cell in neutral or alkaline media would further decrease the carbon efficiency. This issue can be avoided using a proton exchange membrane-based flow cell in acidic medium (Supplementary Fig. 10).

Fig. 3 shows the estimated energy consumptions of a sustainable system to produce 1 mole of CO and ethylene assuming a current density of 200 $mA \cdot cm^{-2}$ (for methods, see Supplementary Note 1: Carbon Efficiency and Energy Consumption Estimation). The one-electron reduction of CO_2, the first step of CO_2 reduction without the involvement of protons, has been shown to be the rate determining step (RDS) of CO formation on Au[4,6,14] and single-atom catalysts.[7] Consequently, the formation rate of CO was pH-independent on the standard hydrogen electrode (SHE) scale. The CO-CO coupling step was found to be the RDS of the reactions that lead to C_2 products on Cu-based catalysts.[20,27-29] Over a long potential window, the CO coverage is relatively saturated,[30] leading to a pH-independent formation rate of C_2

products on the SHE scale. In our experiments, the partial current density-potential (vs. SHE) plots of these products at different pHs were indeed close to each other (within a range of 100 mV) (Supplementary Fig. 11). As the equilibrium potentials of CO_2/CO and CO_2/ethylene are constant on the RHE scale, the overpotential increases as pH decreases. Thus, the energy consumption due to overpotential loss at the cathode is in the order of acidic > near neutral > alkaline. Despite this, the overall energy consumption is the lowest in acidic medium (Fig. 3) thanks to lower losses in other categories. In alkaline medium the regeneration of KOH electrolyte is most energy demanding, leading to an overall energy consumption that is 3 times of that in acidic medium. In near neutral medium, the Ohmic (Supplementary Fig. 12a) and anode energy losses (Supplementary Fig. 12b) were higher than those in acidic medium, leading to an overall energy consumption that is about 14% higher than that in acidic medium.

Cation effect

To understand how K^+ further suppressed HER on SnO_2, Au and Cu in strongly acidic solutions, we measured linear sweeping voltammetry (LSV) curves of a polycrystalline Au rotating disk electrode (RDE) in different electrolyte solutions (Fig. 4a). The onset potential of HER in 0.1 M HOTf + 0.4 M KOTf was close to that in HOTf solution (0.1 M or 0.5 M), while in the K^+-containing solution, a diffusion-limitation feature was observed as a plateau of current density appeared from -0.6 V vs SHE. The current density increases again at -1.3 V vs SHE, close to the onset potential of HER in 0.4 M KOTf, indicating reduction of water molecules started at this potential. The plateau was about 6% higher than the limiting diffusion current density of hydronium reduction calculated according to the Levich equation. In sharp contrast, in 0.1 M HOTf, no plateau of HER current density was observed. To probe the possibility that some unknown impurities that came with KOTf suppressed HER,[31] we prepared a 0.1 M HOTf + 0.4 KOTf solution by partially neutralizing HOTf with an electronic grade KOH (99.999% pure). The LSV curves collected in this solution (Supplementary Fig. 13) overlapped well with the LSV curves in Fig. 4a, supporting that K^+ ions instead of unknown impurities suppressed the HER. LSV curves of SnO_2/C on glassy carbon RDE (Supplementary Fig. 14) and CV curves of SnO_2/C on GDE in N_2 atmosphere (Fig. 1a) show similar trends to curves in Fig. 3a, indicating the suppression of HER by K^+ in strongly acidic medium is a universal effect.

We next probed whether other alkali cations such as Li^+, Na^+ and Cs^+ have the similar effect on the competition between HER and CO_2 reduction as K^+. Indeed, in 0.1 M HOTf + 0.4 M MOTf (M = Li, Na, Cs), plateaus with similar current density were observed (Supplementary

Fig. 14), indicating that these alkali cations also suppressed the migration of hydronium ions. We then measured CO_2 electroreduction on SnO_2/C and Cu/C in acidic solutions containing these alkali cations (Supplementary Fig. 15-17). All alkali cations promoted CO_2 reduction by inhibiting HER, but the effects are variable. On SnO_2/C, the Faradaic efficiency of CO_2 reduction increased in the order Li < Na < K < Cs for both catalysts (Fig. 4b), and the partial current densities of formic acid and CO increased in the same order (Fig. 4c). On Cu/C, the partial current density of ethylene increased in a similar order of Li < Na < K ≈ Cs (Supplementary Fig. 17).

Mechanistic study of cation effect

To probe how alkali cations suppressed the reduction of hydronium ions, we conducted a simulation based on the Poisson-Nernst-Planck model (PNP) which includes migration as one of the mechanisms for mass tranport.[32] Hydronium ions, K^+ and OTf^- were considered, and the reduction of hydronium ions was regarded as the only source of HER in strongly acidic media. The HER current density was assumed proportional to the concentration of hydronium ions in the OHP and exponential to the electrode potential. The simulation reproduced the features of HER at potentials more positive than the onset of reduction of water (Supplementary Fig. 18): in a K^+-free solution, the current density of hydronium reduction increased without any limitation as the potential went cathodically; in a K^+-containing solution, a plateau with a limiting current appeared. The limiting current density was slightly higher (~18%) than the plateau of current density observed in our RDE experiment (Fig. 4a). The small difference was attributed to the neglecting the steric effect of cations in our PNP model.

Fig. 5a and 5b show the profiles of potential and electric field strength with and without K^+ ions. The addition of K^+ ions led to a stronger electric field in the Stern layer and a weaker electric field at >2 nm away from the cathode (inset of Fig. 5b). Hydrated K^+ ions and hydronium ions showed competitive adsorption at the OHP of the cathode. The electric fields generated by the cathode and by these cations at OHP were in the same direction in the Stern layer while opposite in the diffuse layer (Fig. 5c). Although hydronium ions accumulated at OHP had a similar effect to K^+ on the electric field distribution, the effect was weak since hydronium ions at OHP were consumed in HER (Fig. 5d). Hence, in K^+-free medium, the electric field was not sufficiently confined within a few nm from the cathode and the migration of hydronium ions under electric field facilitated the refilling of hydronium ions to OHP. The concentration of hydronium ions at OHP did not change significantly as the electrode potential

shifted cathodically (Supplementary Fig. 19a-b), indicating hydronium ions would not be depleted as current density increased. In K^+-containing medium, due to the competitive adsorption of hydrated K^+ ions against hydronium ions at OHP, a chemically inert hydrated K^+ layer formed at OHP and shielded the electric field from cathode in a long potential window. Thus, the migration of hydronium ions was significantly suppressed. As the electrode potential was more negative, more hydrated K^+ ions accumulated at OHP and concentration of hydronium ions at OHP decreased (Supplementary Fig. 19c-d). Therefore, only in an alkali cation-containing medium depletion of hydronium ions near the cathode would occur, leading to diffusion-limiting like LSV curves in Fig 4a.

For CO_2 reduction in aqueous media, the adsorbed CO_2 (CO_{2ad}) is regarded as a key intermediate.[7,14,20,33,34] Stabilization of CO_{2ad} on the surface of catalysts promotes the production of CO and formate.[14,20,23,34-36] The two C=O bonds of CO_{2ad} bend away from the surface, endowing CO_{2ad} with a large dipole moment oriented outwards.[18,37] Thus, the electric field in Stern layer stabilizes CO_{2ad} (Fig. 5d). Similarly, OCCO intermediate, a key intermediate for the formation of ethylene and ethanol on Cu-based catalyst, has a large outwards dipole moment and is stabilized by the electric field in Stern layer.[18,20,27,38,39] Therefore, K^+ ions not only suppressed HER by impeding the migration of hydronium ions in the diffuse layer, but also promoted CO_2 electroreduction due to the interaction between electric field and dipole moment of adsorbed intermediates.

The cation effect on the pH near the cathode was further explored by the PNP modeling. Hydronium ion reduction, OH- generation from CO_2 reduction, homogeneous reaction between hydronium ions and OH^- ions and the dissociation of water molecules were included in the simulation. Fig. 6a compares the pH profiles in 0.1 M HOTf and 0.1 M HOTf + 0.4 M KOTf media at -0.7 V vs PZC. In K^+-containing medium, the current density of hydronium reduction at this potential was 90 $mA \cdot cm^{-2}$, lower than the limiting diffusion current density at this condition (171 $mA \cdot cm^{-2}$ when the rotating speed of RDE is 400 rpm), implying hydronium ions near the cathode were far from being depleted. As a result, the pH of this solution only increased slightly as approaching OHP (black curve in Fig. 6a). When the distance to OHP was smaller than 2 nm, the pH dropped because hydronium ions were attracted by the negatively charged cathode. In K^+-free medium, the current density of hydronium reduction at -0.7 V vs PZC was 524 $mA \cdot cm^{-2}$, significantly higher than the limiting diffusion current density. In the recent study of Huang et al. on CO_2 reduction in strongly acidic medium,[16] it was hypothesized that cathodic current density higher than 200 $mA \cdot cm^{-2}$ would lead to a pH increase near the cathode. However,

in our simulation (orange curve in Fig. 6a), current density even higher than 500 $mA \cdot cm^{-2}$ did not raise the local pH near the cathode in K^+-free medium. The pH at OHP in K^+-free medium was lower than 0. This was ascribed to the fact that the electric field was not effectively shielded in the absence of inert cations in diffuse layer. Fig. 6b further compares the pH profiles in the two media as the reduction current densities were both around 200 $mA \cdot cm^{-2}$. In K^+-containing medium, we observed the pH increase as approaching OHP. The pH reached the maximum (pH = 6.3) at 2 nm from OHP and dropped as further approaching OHP. Nevertheless, the pH at OHP (pH = 5.1) was still considerably higher than the bulk medium (pH = 1.0). In K^+-free medium, pH did not vary much as approaching OHP and it dropped steeply as the distance to OHP is smaller than 5 nm. Several studies have proposed that the local pH increase at the cathode-electrolyte interface is essential to promote CO_2 reduction over HER.[14-16,19,40] However, our simulation results indicate that inert alkali cations are indispensable for the interfacial pH increase at high current densities.

In our experiment, the partial current density of CO_2 reduction on SnO_2/C in 0.1 M HOTf + 0.4 M KOTf largely exceeded the plateau of HER current density under this condition (Supplementary Fig. 20), implying water was the proton source for CO_2 reduction and OH^- ions were generated from CO_2 reduction. These OH^- ions were expected to react with hydronium ions near the cathode, leading to an further increase of local pH and a decrease of the current density of hydronium reduction.[15] Fig. 6c shows the pH at OHP and Fig. 6d shows the simulated partial current densities of hydronium reduction and CO_2 reduction at different potentials in K^+-containing medium. As CO_2 reduction started to occur, hydronium reduction got suppressed due to the generation of OH^- from CO_2 reduction. This result agrees with our experimental observation (Supplementary Fig. 20). Thanks to this local pH effect in the presence of an inert cation, the Faradaic efficiency of CO_2 reduction could reach as high as 90% for SnO_2/C and Au/C catalysts (Fig. 1b, d). Supplementary Fig. 21c compares the simulated pH profiles in K^+-containing medium at -1.26 V vs PZC with and without OH^- generation from CO_2 reduction. The maximum pH appeared at 2 nm from OHP in both cases, with the pH value of 6.3 and 5.5, respectively. This result indicates the local pH increase in K^+-containing medium was mainly due to the effective shielding of electric field by alkali cations, and the generation of OH^- ions from CO_2 reduction further increased the local pH by 0.8 units.

The effect of different alkali cations[18-20,38,41] and quaternary ammonium cations[42,43] on CO_2 reduction was extensively studied in near neutral and alkaline media. In alkali cation-containing media, the activity of CO_2 reduction to CO and ethylene was highest with Cs^+ and

lowest with Li^+, similar to our observation in acidic medium. The size of hydrated cations decreased from Li to Cs. As the size of hydrated cations decreases, more alkali cations can accumulate at the OHP.[18,20,44] According to the model in Fig. 5c, the electric field was more confined in Stern layer as the concentration of cations in OHP increased, and thus, CO_{2ad} and OCCO intermediate was more stabilized and the formation of CO and ethylene was more promoted.

Under N_2, the onset potential and plateau current density for HER were similar with different alkali cations (e.g., Supplementary Fig. 14 for SnO_2/C). Under CO_2, the HER current density was higher with Li^+ or Na^+ than with K or Cs (Fig. 4c and Supplementary Fig. 22). This trend is due to the influence of CO_2 reduction on HER. CO_2 reduction generates OH^- ions, which neutralize hydronium ions. As shown in Fig. 6d**,** a higher CO_2 reduction current density leads to a lower hydronium reduction current density. The current density of CO_2 reduction increases going from Li^+ to Cs^+. Thus, the current density of hydronium reduction should decrease going from Li^+ to Cs^+. This trend was observed on SnO_2/C at -1.14 and -1.24 V (Supplementary Fig. 22). At -1.34 V, the reduction of water in addition to hydronium contributes to HER, which led to the trend in Fig. 4c.

Previous studies showed that methane production and HER followed the same trend for CO_2 reduction on Cu in near neutral and alkaline media,[7,18,45,46] which was attributed to the involvement of water (as proton source) in the RDS of methane formation. For CO_2 reduction on Cu/C in acidic medium containing alkali cations this trend did not hold when the potentials were increased (Fig. 1g). This result can be understood considering the change of proton source in HER at different potentials. At potentials lower than -1.2 V vs. RHE, hydronium ions are the proton source for HER; at higher potentials, water becomes an additional proton source. On the other hand, water is the proton source for CO_2 reduction at all potentials (see above).

The double layer effects in electrokinetics have long been studied.[47] Earlier work proposed that alkali cations accumulated at OHP shielded the electric field, decreasing the force for outward migration of anions from the cathode.[48,49] We show here that a similar effect can suppress migration of hydronium towards the cathode, thereby disfavoring HER. This effect can be exploited to conduct efficient CO_2 electroreduction in strongly acidic medium. Our work is a further demonstration that electrocatalysis can be controlled by modulating the electric field near the electrode.

Conclusions

By using alkali cations to suppress hydronium reduction and promote CO_2 reduction, we demonstrated efficient CO_2 electroreduction in strongly acidic medium. We showed that this approach is universal for various catalysts and cations, and we revealed cation-induced modulation of electric field as the origin of the cation effects. This work provides a promising strategy to avoid the carbonate problem in CO_2 electroreduction, which is one of the main road blocks for low-temperature CO_2 electrolysis.

Methods

Preparation of catalysts

Carbon black (Vulcan XC-72R), anhydrous tin(II) chloride ($SnCl_2$, 98%, Acros), sodium oxalate ($Na_2C_2O_4$, 99.5%, Sigma-Aldrich), hydrochloric acid (HCl, 37%, VWR international SA), gold(III) chloride hydrate ($HAuCl_4 \cdot xH_2O$, 99.999%, Sigma-Aldrich), oleylamine (approximate C18-content 80-90%, Acros), borane tert-butylamine complex (BTB, 97%, Sigma-Aldrich), copper(II) acetylacetonate ($Cu(acac)_2$, 98%, Acros) and trioctylphosphine oxide (TOPO, 99%, Sigma-Aldrich) were used as received without further purification. Deionized water (18 MΩ·cm) obtained from a Milli-Q integral water purification system (Merck Millipore Corporation) was used for all experiments.

SnO_2/C was synthesized by a method modified from literature.[50] 120 mg of nitric acid-treated carbon black was dispersed in 10 mL of deionized water, and 200 μL of HCl (37%) was added. 190 mg of anhydrous $SnCl_2$ was added into the dispersion under vigorous stirring. After 30 seconds, 10 mL of 0.2 M $Na_2C_2O_4$ solution was added quickly and the dispersion was kept under stirring at 25 °C for 30 minutes. SnC_2O_4/C was then collected by centrifugation, washed by deionized water for three times, and dried under vacuum at 25 °C. The as-synthesized SnC_2O_4/C was then loaded in a corundum crucible and put into a muffle. The sample was heated to 400 °C in air with a ramping rate of 5 °C·min^{-1}, and kept at 400 °C for 4 h. After the sample cooled naturally to room temperature, SnO_2/C was obtained. Supplementary Fig. 1a and 1b show the high angle annular dark field-scanning transmission electron microscopy (HAADF-STEM) image and powder X-ray diffraction (PXRD) pattern of SnO_2/C.

Au/C was synthesized with a method modified from literature.[51] 50 mg of $HAuCl_4 \cdot xH_2O$, 125 μL of toluene and 30 mg of carbon black were added into 10 mL of oleylamine, and the mixture was stirred at 600 rpm for 10 minutes under N_2 atmosphere. 22.5

mg of BTB was dissolved in 2.5 mL of oleylamine and this solution was rapidly injected into the above-mentioned mixture. The resulting mixture was stirred at 25 °C under N_2 for 1 h. Then, 15 mL of ethanol was added into the mixture. A black powder was separated from the reaction mixture by centrifugation, washed by toluene-ethanol mixed solvent (v:v = 1:1) twice, and dried at 70 °C. Finally, the powder was heated at 185 °C in air overnight to give the final sample of Au/C. Supplementary Fig. 1c and 1d show the HAADF-STEM image and PXRD pattern of Au/C.

Cu/C was synthesized with a method modified from literature.[52] 0.196 g of $Cu(acac)_2$ and 2.90 g of TOPO were dissolved in 35 mL of oleylamine and 100 mg of carbon black was added into this solution. The mixture was evacuated at 80 °C for 15 minutes, and then rapidly heated to 200 °C under N_2 atmosphere. The reaction was kept at 200 °C for 1 h and then cooled to room temperature naturally. 40 mL of ethanol was then added into the mixture and a black solid was separated from the reaction mixture by centrifugation. This crude product was washed with *n*-hexane-ethanol mixed solvent (v:v = 1:1) twice, and dried under vacuum at room temperature to give the final sample of Cu/C. Cu/C was stored in glove box with N_2 to prevent the oxidation of Cu. Supplementary Fig. 1e and 1f show the HAADF-STEM image and PXRD pattern of Cu/C.

Characterizations

PXRD patterns were collected on an Aeris diffractometer (PANalytical) with monochromatic Cu Kα radiation. HAADF-STEM images were collected on an FEI Talos TEM operated at 200 kV with high brightness XFEG gun. X-ray photoelectron spectroscopy (XPS) characterizations were performed on a PHI5000 VersaProbe II XPS system by Physical Electronics (PHI) with a detection limit of 1 at%. Monochromatic x-rays were generated by an Al Kα source (1486.7 eV). ICP-MS results were obtained by a NexIon 350 (Perkin Elmer) machine.

Electrochemical measurements

All electrochemical measurements were carried out on a Gamry Reference 3000 electrochemical instrument. Current-interrupt *iR* compensation was used unless otherwise noted. Ag/AgCl | saturated KCl electrode was used as the reference electrode. Potential of working electrode versus SHE was calculated according to:

$$E(\text{vs SHE}) = E(\text{vs Ag/AgCl}) + 0.197\ \text{V} \quad (1)$$

Potential versus RHE was calculated according to:

$$E(\text{vs RHE}) = E(\text{vs SHE}) + 0.0592\ \text{V} \times \text{pH} \quad (2)$$

The pH value of electrolyte was measured by pH meter (HI 991002, Hanna instruments).

The performance of CO_2 reduction was tested in a home-made flow cell shown in Supplementary Fig. 2. The left part, made of stainless steel, was used as the current collector of the working electrode and the gas chamber of CO_2 stream behind GDE. The two PEEK parts were the chambers for electrolyte solutions for the working and counter electrodes. The window for the effective area was set to 1 cm × 1 cm. The thickness of each chamber was 1 cm. Each chamber has an inlet and an outlet for electrolyte. The reference electrode was inserted in the chamber of the working electrode. Nafion® 211 membrane was used to separate the counter electrode from the chamber of the working electrode. Titanium plate with a window (1 cm × 1 cm) was used as the current collector for the counter electrode. PTFE films were used as gaskets. All parts were pressed together by four sets of screws and nuts.

To prepare the catalyst ink of SnO_2/C, Au/C and Cu/C, 20 mg of catalyst, 4 mL of ethanol and 200 μL of Nafion® dispersion (5%, ABCR) were mixed and sonicated for 30 minutes. CeTech carbon cloth with a micropore layer on one side (W1S1009) was used as the GDE. The carbon cloth was cut into 3 cm × 3 cm square, mounted on a vertically placed heating plate and heated to 120 °C. The ink was sprayed onto the micropore-layer side of the carbon cloth by air-brush. The carbon cloth was then cut into 4 pieces (1.5 cm × 1.5 cm) as the working electrodes. Iridium(IV) oxide (IrO_2, 99%, ABCR) sprayed on ELAT hydrophilic carbon cloth was used as the catalyst for the counter electrode. The ink of IrO_2 containing 20 mg of IrO_2, 4 mL of ethanol, and 40 μL of Nafion® dispersion. When we tested Cu/C in 0.1 M H_2SO_4 + 0.4 M K_2SO_4 and 0.1 M H_2SO_4 + 0.4 M Cs_2SO_4, half of the electrode was covered by Kapton tape and the effective area of the electrode was 0.5 cm^2. The effective area of electrode in all the other cases was 1 cm^2.

The potential dependent CO_2 reduction properties were tested in the three-electrode flow cell with chronoamperometry method. The volumes of both catholyte and anolyte solutions were 14 mL, and both of them were circulated with a flow rate of 5 $mL \cdot min^{-1}$. The flow rate was controlled by a peristaltic pump (REGLO Digital MS-4/8, Ismatec). The humidified CO_2 was connected to the inlet of the gas chamber and the outlet was connected to gas chromatography (GC) for online detection of gas-phase products. The flow of CO_2 was controlled by a mass flow controller (Red-y smart series, Vögtlin) in the range ≤ 50 standard

cubic centimeters per minute (sccm) and by another mass flow controller (EL-FLOW, Bronkhorst) in the range between 50 and 200 sccm. The flow rate of CO_2 was adjusted according to current as shown in Supplementary Fig. 5a. The duration of one chronoamperometry test was 30 minutes. The online GC sampling was at 10 minutes. 400 μL of electrolyte solution was taken after each chronoamperometry test for ^{1}H-nuclear magnetic resonance (^{1}H-NMR) test to quantify the products dissolved in electrolyte. Current densities were averaged over 30 minutes. The error bars of Faradaic efficiency and partial current density were standard deviations based on tests of 3 individual working electrodes.

RDE experiment was done by using a gold or a glassy carbon RDE (Autolab) with a diameter of 5 mm. Before experiments, the electrode was polished by alumina polishing powder (0.05 μm). To prepare the catalyst ink, 5 mg of SnO_2/C, 1 mL of deionized water, 250 μL of isopropanol, and 50 μL of Nafion® dispersion were mixed and sonicated for 30 minutes. 20 μL of the ink was drop-cast on the RDE and dried under N_2 flow. The tests were conducted in a three-neck flask. The RDE was inserted inclinedly from the right side of the flask, facilitating the bubbles generated on the RDE to escape (Supplementary Fig. 23 and Supplementary Video 1). The reference electrode was put in a Luggin capillary and the distance between the tip of the capillary and RDE was 5 mm. A platinum wire was used as the counter electrode. The electrolyte was saturated with N_2. Linear sweeping voltammetry curves were collected with a scan rate of 5 $mV \cdot s^{-1}$. The resistance of electrolyte was determined by high-frequency impedance measurements and *iR* compensation was done after experiment.

More detailed procedures of electrochemical measurements were in Supplementary Methods.

Poisson-Nernst-Planck simulation

The one-dimensional steady-state profiles of concentrations of hydronium ions, K^+ ions and OTf^- ions and the profile of potential were obtained from PNP simulation. The domain for simulation was divided into two regions. The first region was between the surface of cathode and OHP, which is called Stern layer. The second region was between OHP and bulk electrolyte, with a thickness of 100 nm, containing diffuse layer and diffusion layer. Diffusion, migration and convection induced by RDE were considered in the simulation, and the potential profile needed to fulfill Poisson equation. Boundary conditions at the surface of cathode, OHP and the bulk-electrolyte side were used to solve the equations (Supplementary Fig. 24). Hydronium ion reduction, OH^- generation from CO_2 reduction, the neutralization reaction between OH^- and

hydronium ions, and dissociation of water molecules were subsequently included in the simulation of interfacial pH (Supplementary Fig. 25). The coupled equations were solved with a commercial solver (COMSOL 5.5) utilizing a MUMPS solver with a non-linear automatic Newton method. The detailed equations, boundary conditions, and parameter settings were in Supplementary Note 2: Simulation Procedure.

Data availability

Data that support the findings of this study can be found in the article and the Supplementary Information; this information is also available from the corresponding author upon request. Datasets of Fig. 1-6 can be found in Zenodo.[53]

Acknowledgements

The authors thank Dr. Lichen Bai for the help in TEM characterizations and Mr. Haigang Qin for the help in XPS characterizations and RDE tests. **Funding:** This work was supported by the European Research Council (681292, X.H), NCCR Catalysis (180544, X.H. and S.H.), a National Centre of Competence in Research funded by the Swiss National Science Foundation, the EPFL(X.H. and S.H.), Foundation of Shenzhen Science, Technology and Innovation Commission (SSTIC) (JCYJ20210324104414039, J.G.), the European Union Marie Sklodowska-Curie Individual Fellowships (891545, W.R.), the European Union's Horizon 2020 research and innovation programme (85144, SELECT-CO2, S.H.), and a Starting Grant of the Swiss National Science Foundation (155876, S.H.).

Author contributions

J.G. performed the majority of the synthesis, characterization, and electrochemical tests. S.L. performed the simulations. W.N. performed the Au rotating disk electrode tests. W.R. performed the electrochemical tests in near neutral and alkaline media. J.G., S.L., S.H. and X.H. analyzed the data. J.G. and X.H. wrote the paper, with input from all other co-authors. S.H. and X.H. directed the research.

Competing interests

The authors declare no competing interests.

Tables

Table 1. Theoretical carbon efficiency of CO_2 reduction to generate CO, formic acid (or formate) and ethylene in a flow cell in acidic, near neutral, or alkaline medium and an MEA setup with an anion exchange membrane. [a]

Product	Acidic	Neutral	Alkaline [b]	MEA
CO	100%	50%	11.7%	50%
Formic acid (or formate)	100%	50%	11.7%	<50% [c]
Ethylene	100%	25%	4.2%	25%

a. Theoretical carbon efficiency was estimated by assuming all CO_2 is consumed at the cathode to form reduction products or carbonate and the Faradaic efficiency of the desired product is 100%.

b. Assuming a constant reaction rate between CO_2 and OH^- ions at the gas-electrolyte interface and a current density of 200 $mA \cdot cm^{-2}$. See Supplementary Note 1 for the methods.

c. Formate anions penetrate the membrane and may be oxidized at the anode, leading to a decrease in carbon efficiency.

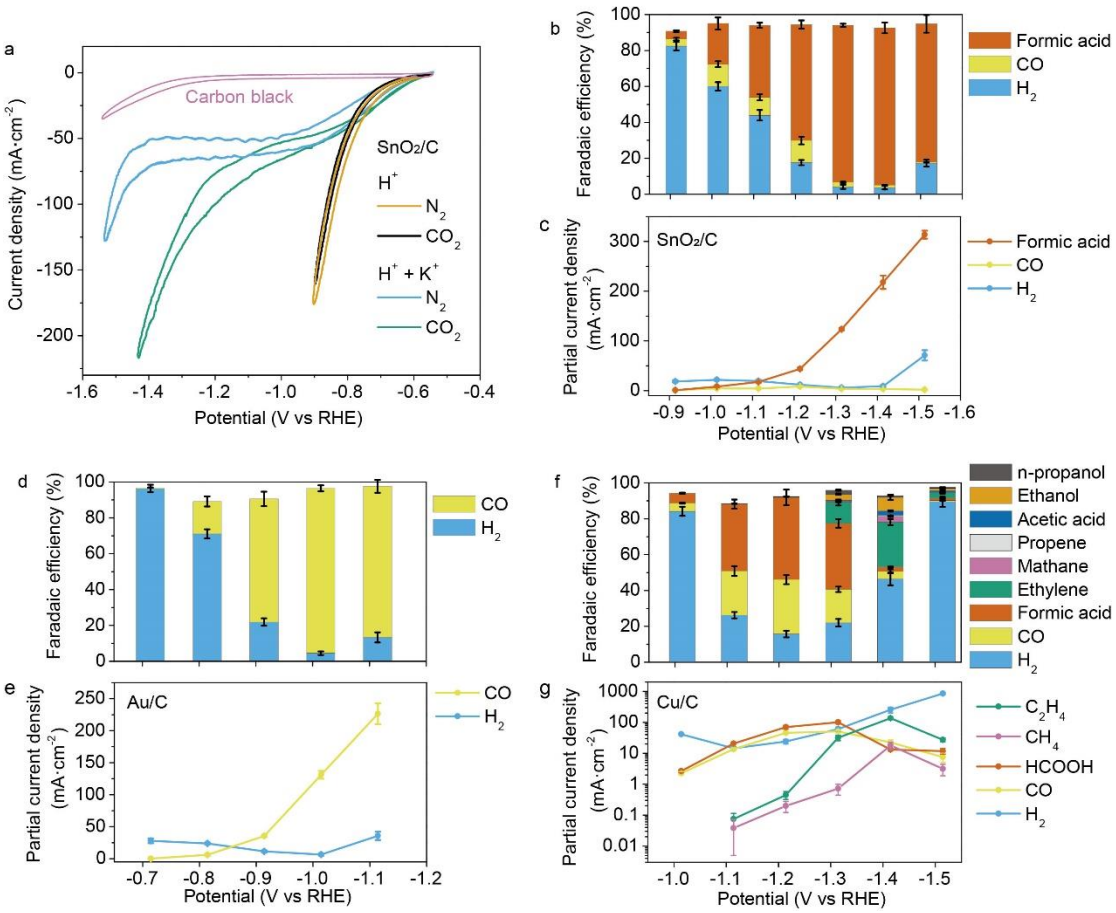

Fig. 1. Performance of CO_2 reduction in acidic solutions containing K^+ ions. (a) CV curves of SnO_2/C in 0.1 M HOTf with N_2 (orange) and CO_2 (black), in 0.1 M HOTf + 0.4 M KOTf with N_2 (blue) and CO_2 (green), and CV curve of Vulcan XC-72R in 0.1 M HOTf + 0.4 M KOTf with CO_2 (light pink). Scan rate was 20 $mV \cdot s^{-1}$. (b, d, f) Faradaic efficiency and (c, e, g) partial current density of different reduction products in 0.1 M H_2SO_4 + 0.4 M K_2SO_4. The catalysts were (b, c) SnO_2/C, (d, e) Au/C and (f, g) Cu/C. The partial current densities of minor products on Cu/C are not shown in panel (g). Error bars were standard deviations based on tests of 3 individual working electrodes.

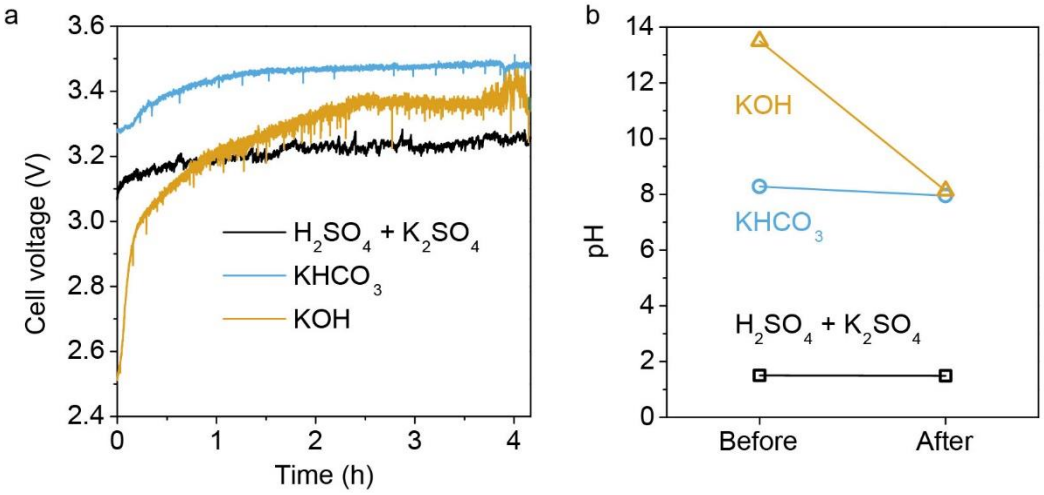

Fig. 2. Comparison of CO_2 electroreduction in acidic, near neutral and alkaline media. (a) Cell voltage of two-electrode flow cells with Au/C and IrO_2 as catalysts for cathode and anode, respectively. The current density was 200 $mA \cdot cm^{-2}$. No *iR* compensation was applied. Electrolytes: 0.1 M H_2SO_4 + 0.4 M K_2SO_4 (black), 0.8 M $KHCO_3$ (blue), and 0.8 M KOH (orange). (b) The pH values of electrolyte solutions before and after electrolysis.

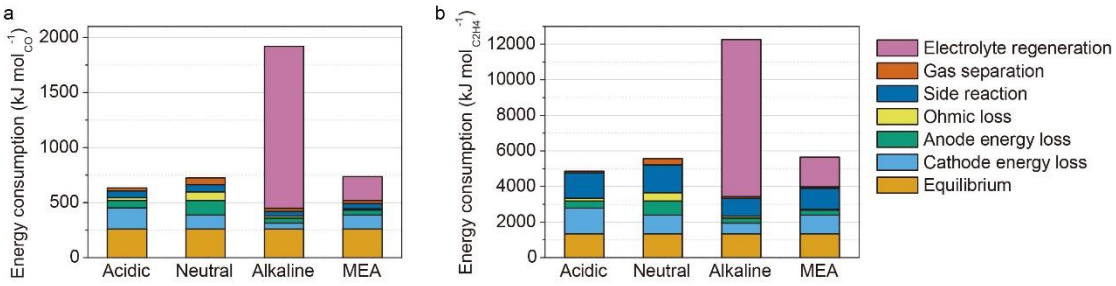

Fig. 3. Estimation of energy consumption for sustainable CO_2 electroreduction. Energy consumption to produce 1 mole of (a) CO and (b) ethylene, assuming a partial current density of 200 mA·cm^{-2}. Systems based on a flow cell with acidic, near neutral, or alkaline medium, and an MEA with an anion exchange membrane are compared.

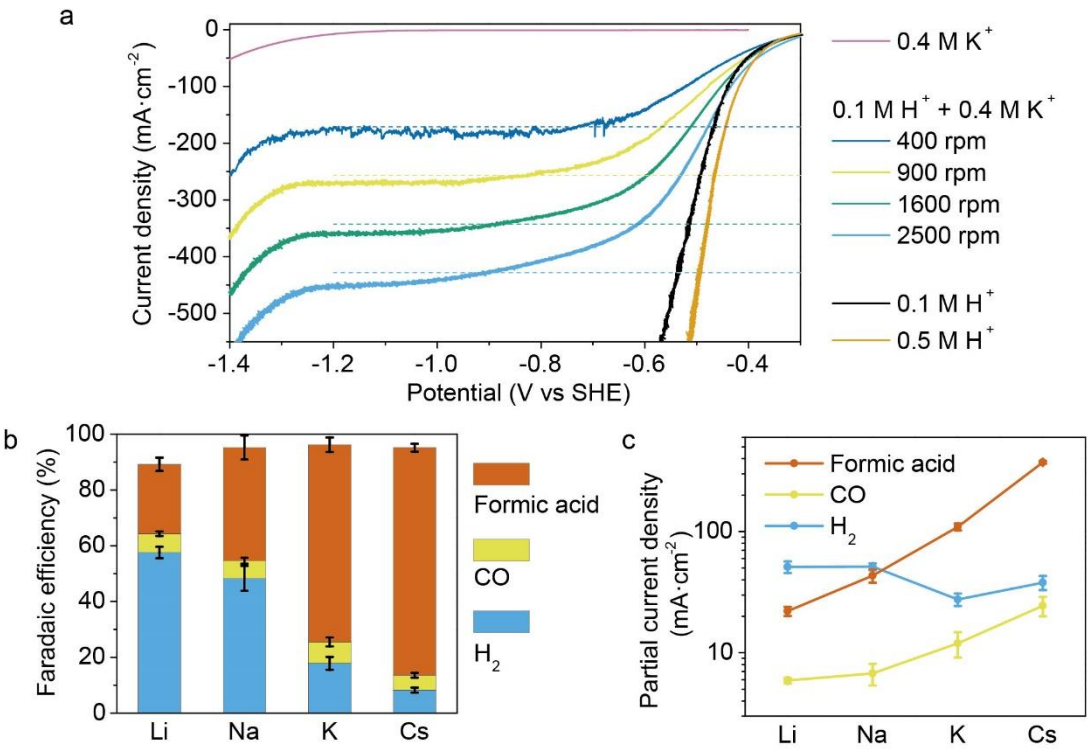

Fig. 4. Cation effects on HER and CO_2 reduction. (a) LSV curves of Au RDE in N_2 saturated solutions: 0.1 M HOTf + 0.4 M KOTf (dark blue, yellow, green and light blue curves were collected with the rotating speed of 400, 900, 1600, and 2500 rpm, respectively), 0.4 M KOTf (light pink, 1600 rpm), 0.1 M HOTf (black, 1600 rpm) and 0.5 M HOTf (orange, 1600 rpm). The horizontal dashed lines indicate the limiting diffusion current densities of the reduction of hydronium ions at the corresponding rotating speed calculated from the Levich equation. (b) Faradaic efficiency and (c) partial current densities of formic acid, CO and H_2 of SnO_2/C in 0.1 M HOTf + 0.4 M MOTf (M = Li, Na, K and Cs) at -1.34 V vs RHE. Error bars were standard deviations based on tests of 3 individual working electrodes.

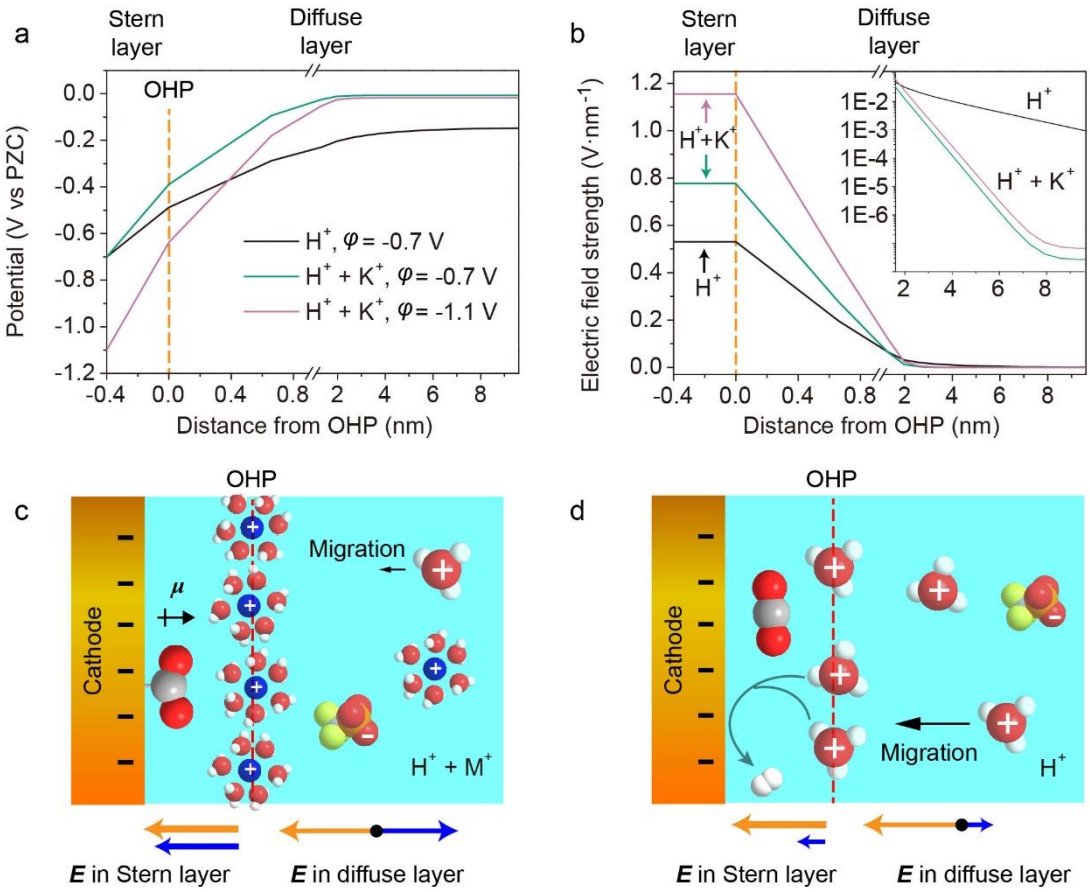

Fig. 5. Cation effects on electric field distribution. Simulated (a) potential and (b) electric field strength profiles over the distance from OHP. The direction of electric field was towards the cathode. The surface of electrode was at x = -0.4 nm. The orange dashed lines at x = 0 nm represent OHP. Black curves show the profiles of 0.1 M HOTf with the electrode potential of -0.7 V vs potential of zero charge (PZC). Green and light pink curves show the profiles of 0.1 M HOTf + 0.4 M KOTf with the electrode potential of -0.7 V and -1.1 V vs PZC, respectively. The rotating speed was 400 rpm in the simulation. At -1.1 V vs PZC, the HER current density reached the plateau. The inset of panel (b) shows the magnification of the electric field strength profile between 1.6 nm and 9.6 nm. Schemes of double layer near cathode in (c) HOTf + MOTf and (d) HOTf media. Grey, red, white, blue, yellow and orange balls represent C, O, H, K, F and S atoms, respectively. Orange arrows represent electric field (E) generated by the cathode and blue arrows represent E generated by cations at OHP. In panel (c), μ represent the dipole moment of adsorbed CO_2 intermediate. In panel (d), hydronium ions at OHP are consumed by HER.

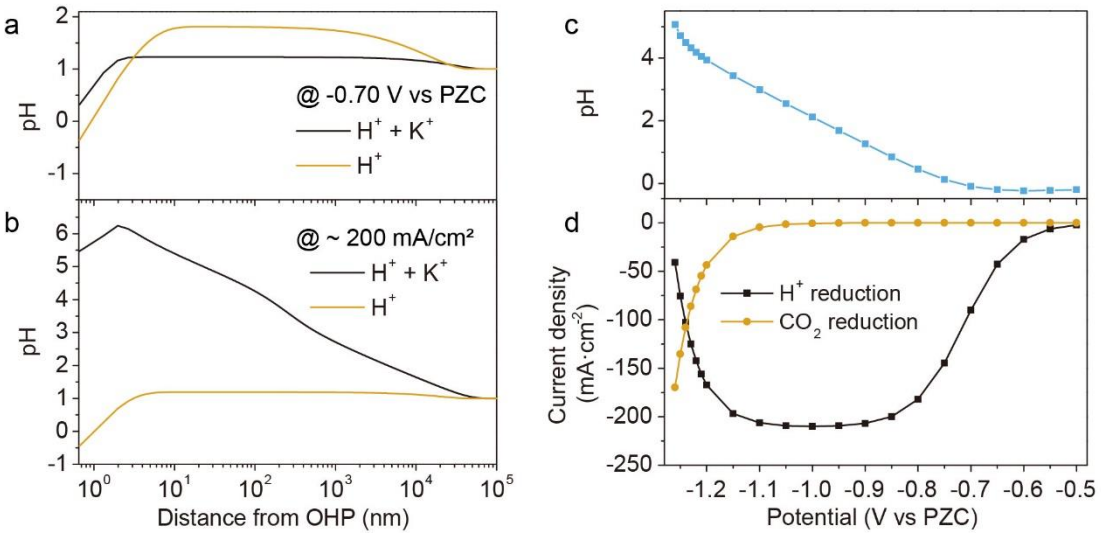

Fig. 6. Simulation of local pH effect. (a) pH profiles over distance from OHP in 0.1 M HOTf + 0.4 M KOTf (black curve) and in 0.1 M HOTf (orange curve) at -0.70 V vs PZC. The corresponding cathodic current densities were 90 mA·cm^{-2} and 524 mA·cm^{-2}, respectively. (b) pH profiles in 0.1 M HOTf + 0.4 M KOTf with cathodic current density of 211 mA·cm^{-2} (black curve) and in 0.1 M HOTf with cathodic current density of 221 mA·cm^{-2} (orange curve). The corresponding potentials were -1.26 V vs PZC and -0.65 V vs PZC, respectively. (c) pH at OHP and (d) partial current densities of hydronium reduction (black curve) and CO_2 reduction (orange curve) at different potentials in 0.1 M HOTf + 0.4 M KOTf medium.

References

1 Chu, S., Cui, Y. & Liu, N. The path towards sustainable energy. *Nat. Mater.* **16**, 16-22, (2017).

2 Verma, S. *et al.* Insights into the low overpotential electroreduction of CO_2 to CO on a supported gold catalyst in an alkaline flow electrolyzer. *ACS Energy Lett.* **3**, 193-198, (2018).

3 Dinh, C.-T., García de Arquer, F. P., Sinton, D. & Sargent, E. H. High rate, selective, and stable electroreduction of CO_2 to CO in basic and neutral media. *ACS Energy Lett.* **3**, 2835-2840, (2018).

4 Zhang, B. A., Ozel, T., Elias, J. S., Costentin, C. & Nocera, D. G. Interplay of homogeneous reactions, mass transport, and kinetics in determining selectivity of the reduction of CO_2 on gold electrodes. *ACS Centr. Sci.* **5**, 1097-1105, (2019).

5 Rabinowitz, J. A. & Kanan, M. W. The future of low-temperature carbon dioxide electrolysis depends on solving one basic problem. *Nat. Commun.* **11**, 5231, (2020).

6 Wuttig, A., Yaguchi, M., Motobayashi, K., Osawa, M. & Surendranath, Y. Inhibited proton transfer enhances Au-catalyzed CO_2-to-fuels selectivity. *Proc. Natl. Acad. Sci.*

113, E4585-E4593, (2016).
7 Varela, A. S. *et al.* pH effects on the selectivity of the electrocatalytic CO_2 reduction on graphene-embedded Fe–N–C motifs: Bridging concepts between molecular homogeneous and solid-state heterogeneous catalysis. *ACS Energy Lett.* **3**, 812-817, (2018).
8 Ozden, A. *et al.* Cascade CO_2 electroreduction enables efficient carbonate-free production of ethylene. *Joule* **5**, 706-719, (2021).
9 Hori, Y. Electrochemical CO_2 reduction on metal electrodes, in *Modern Aspects of Electrochemistry* 89-189 (Springer, 2008).
10 Zhu, D. D., Liu, J. L. & Qiao, S. Z. Recent advances in inorganic heterogeneous electrocatalysts for reduction of carbon dioxide. *Adv. Mater.* **28**, 3423-3452, (2016).
11 Ma, M. *et al.* Insights into the carbon balance for CO_2 electroreduction on Cu using gas diffusion electrode reactor designs. *Energy Environ. Sci.* **13**, 977-985, (2020).
12 Wang, J., Xu, F., Jin, H., Chen, Y. & Wang, Y. Non-noble metal-based carbon composites in hydrogen evolution reaction: fundamentals to applications. *Adv. Mater.* **29**, 1605838, (2017).
13 Shao, Y., Xiao, X., Zhu, Y.-P. & Ma, T.-Y. Single-crystal cobalt phosphate nanosheets for biomimetic oxygen evolution in neutral electrolytes. *Angew. Chem. Int. Ed.* **58**, 14599-14604, (2019).
14 Ringe, S. *et al.* Double layer charging driven carbon dioxide adsorption limits the rate of electrochemical carbon dioxide reduction on Gold. *Nat. Commun.* **11**, 33, (2020).
15 Bondue, C. J., Graf, M., Goyal, A. & Koper, M. T. M. Suppression of hydrogen evolution in acidic electrolytes by electrochemical CO_2 reduction. *J. Am. Chem. Soc.* **143**, 279-285, (2021).
16 Huang, J. E. *et al.* CO_2 electrolysis to multicarbon products in strong acid. *Science* **372**, 1074-1078, (2021).
17 Monteiro, M. C. O. *et al.* Absence of CO_2 electroreduction on copper, gold and silver electrodes without metal cations in solution. *Nat. Catal.* **4**, 654-662, (2021).
18 Resasco, J. *et al.* Promoter effects of alkali metal cations on the electrochemical reduction of carbon dioxide. *J. Am. Chem. Soc.* **139**, 11277-11287, (2017).
19 Singh, M. R., Kwon, Y., Lum, Y., Ager, J. W. & Bell, A. T. Hydrolysis of electrolyte cations enhances the electrochemical reduction of CO_2 over Ag and Cu. *J. Am. Chem. Soc.* **138**, 13006-13012, (2016).
20 Ringe, S. *et al.* Understanding cation effects in electrochemical CO_2 reduction. *Energy Environ. Sci.* **12**, 3001-3014, (2019).
21 Xia, C. *et al.* Continuous production of pure liquid fuel solutions via electrocatalytic CO_2 reduction using solid-electrolyte devices. *Nat. Energy* **4**, 776-785, (2019).
22 Liu, L.-X. *et al.* Tuning Sn_3O_4 for CO_2 reduction to formate with ultra-high current density. *Nano Energy* **77**, 105296, (2020).
23 Gu, J., Hsu, C.-S., Bai, L., Chen, H. M. & Hu, X. Atomically dispersed Fe^{3+} sites catalyze efficient CO_2 electroreduction to CO. *Science* **364**, 1091-1094, (2019).
24 Li, F. *et al.* Molecular tuning of CO_2-to-ethylene conversion. *Nature* **577**, 509-513, (2020).
25 García de Arquer, F. P. *et al.* CO_2 electrolysis to multicarbon products at activities greater than 1 $A \cdot cm^{-2}$. *Science* **367**, 661-666, (2020).
26 Ma, S. *et al.* One-step electrosynthesis of ethylene and ethanol from CO_2 in an alkaline electrolyzer. *J. Power Sources* **301**, 219-228, (2016).
27 Sandberg, R. B., Montoya, J. H., Chan, K. & Nørskov, J. K. CO-CO coupling on Cu facets: Coverage, strain and field effects. *Surf. Sci.* **654**, 56-62, (2016).
28 Zhan, C. *et al.* Revealing the CO coverage-driven C–C coupling mechanism for

electrochemical CO_2 reduction on Cu_2O nanocubes via operando Raman spectroscopy. *ACS Catal.* **11**, 7694-7701, (2021).

29 Kim, Y. *et al.* Time-resolved observation of C–C coupling intermediates on Cu electrodes for selective electrochemical CO_2 reduction. *Energy Environ. Sci.* **13**, 4301-4311, (2020).

30 Liu, X. *et al.* pH effects on the electrochemical reduction of CO_2 towards C2 products on stepped copper. *Nat. Commun.* **10**, 32, (2019).

31 Wuttig, A. & Surendranath, Y. Impurity ion complexation enhances carbon dioxide reduction catalysis. *ACS Catal.* **5**, 4479-4484, (2015).

32 Newman, J. & Thomas-Alyea, K. E. *Electrochemical Systems*. 3rd edn, (John Wiley & Sons, 2004).

33 Wuttig, A., Yoon, Y., Ryu, J. & Surendranath, Y. Bicarbonate is not a general acid in Au-catalyzed CO_2 electroreduction. *J. Am. Chem. Soc.* **139**, 17109-17113, (2017).

34 Lee, M.-Y., Ringe, S., Kim, H., Kang, S. & Kwon, Y. Electric field mediated selectivity switching of electrochemical CO_2 reduction from formate to CO on carbon supported Sn. *ACS Energy Lett.* **5**, 2987-2994, (2020).

35 Vijay, S. *et al.* Dipole-field interactions determine the CO_2 reduction activity of 2D Fe–N–C single-atom catalysts. *ACS Catal.* **10**, 7826-7835, (2020).

36 Jafarzadeh, A., Bal, K. M., Bogaerts, A. & Neyts, E. C. Activation of CO_2 on copper surfaces: The synergy between electric field, surface morphology, and excess electrons. *J. Phys. Chem. C* **124**, 6747-6755, (2020).

37 Chen, L. D., Urushihara, M., Chan, K. & Nørskov, J. K. Electric field effects in electrochemical CO_2 reduction. *ACS Catal.* **6**, 7133-7139, (2016).

38 Ludwig, T. *et al.* Atomistic insight into cation effects on binding energies in Cu-catalyzed carbon dioxide reduction. *J. Phys. Chem. C* **124**, 24765-24775, (2020).

39 Hedström, S. *et al.* Spin uncoupling in chemisorbed OCCO and CO_2: Two high-energy intermediates in catalytic CO_2 reduction. *J. Phys. Chem. C* **122**, 12251-12258, (2018).

40 Ooka, H., Figueiredo, M. C. & Koper, M. T. M. Competition between hydrogen evolution and carbon dioxide reduction on copper electrodes in mildly acidic media. *Langmuir* **33**, 9307-9313, (2017).

41 Thorson, M. R., Siil, K. I. & Kenis, P. J. A. Effect of cations on the electrochemical conversion of CO_2 to CO. *J. Electrochem. Soc.* **160**, F69-F74, (2012).

42 Zhang, Z.-Q., Banerjee, S., Thoi, V. S. & Shoji Hall, A. Reorganization of interfacial water by an amphiphilic cationic surfactant promotes CO_2 reduction. *J. Phys. Chem. Lett.* **11**, 5457-5463, (2020).

43 Li, J., Li, X., Gunathunge, C. M. & Waegele, M. M. Hydrogen bonding steers the product selectivity of electrocatalytic CO reduction. *Proc. Natl. Acad. Sci.* **116**, 9220-9229, (2019).

44 Bohra, D., Chaudhry, J. H., Burdyny, T., Pidko, E. A. & Smith, W. A. Modeling the electrical double layer to understand the reaction environment in a CO_2 electrocatalytic system. *Energy Environ. Sci.* **12**, 3380-3389, (2019).

45 Choi, C. *et al.* Highly active and stable stepped Cu surface for enhanced electrochemical CO_2 reduction to C_2H_4. *Nat. Catal.* **3**, 804-812, (2020).

46 Li, J. *et al.* Hydroxide is not a promoter of C2+ product formation in the electrochemical reduction of CO on copper. *Angew. Chem. Int. Ed.* **59**, 4464-4469, (2020).

47 Fawcett, W. R. Fifty years of studies of double layer effects in electrode kinetics—a personal view. *J. Solid State Electrochem.* **15**, 1347, (2011).

48 Frumkin, A. N., Petry, O. A. & Nikolaeva-Fedorovich, N. V. On the determination of the value of the charge of the reacting particle and of the constant α from the dependence of the rate of electro-reduction on the potential and concentration of the solution.

Electrochim. Acta **8**, 177-192, (1963).
49 Fawcett, W. R. & Mackey, M. D. The electroreduction of peroxydisulphate anion in formamide. *J. Electroanal. Chem. Interfac. Electrochem.* **27**, 219-231, (1970).
50 Gu, J., Héroguel, F., Luterbacher, J. & Hu, X. Densely packed, ultra small SnO nanoparticles for enhanced activity and selectivity in electrochemical CO_2 reduction. *Angew. Chem. Int. Ed.* **57**, 2943-2947, (2018).
51 Wang, Y. *et al.* Ensemble effect in bimetallic electrocatalysts for CO_2 reduction. *J. Am. Chem. Soc.* **141**, 16635-16642, (2019).
52 Guo, H. *et al.* Shape-selective formation of monodisperse copper nanospheres and nanocubes via disproportionation reaction route and their optical properties. *J. Phys. Chem. C* **118**, 9801-9808, (2014).
53 Gu, J., Liu, S., Ni, W., Ren, W., Haussener, S. & Hu, X. Data of the paper "Modulating electric field distribution by alkali cations for CO_2 electroreduction in strongly acidic medium". *Zenodo* https://doi.org/10.5281/zenodo.5751314 (2021).